

## HYBRID CELL CENTRED/VERTEX MODEL FOR LARGE TISSUE DEFORMATIONS

José J. Muñoz<sup>1</sup>, Payman Mosaffa<sup>1</sup>, Yanlan Mao<sup>2</sup>, Rob Tetley<sup>2</sup>, Nina Asadipour<sup>1</sup> and Antonio Rodríguez-Ferran<sup>1</sup>

<sup>1</sup>Laboratori de Càlcul Numèric (LaCàN), Universitat Politècnica de Catalunya, 08034 Barcelona, Spain  
{j.munoz, payman.mosaffa, nina.asadipour, antonio.rodriguez-ferran}@upc.edu

<sup>2</sup>MRC Laboratori for Molecular Cell Biology, University College London  
{y.mao,r.tetley}@ucl.ac.uk

**Keywords:** Cell-centred, vertex, tissue mechanics, Voronoi, network, wound healing, embryogenesis

**Abstract.** *Macroscopic deformations in embryonic soft tissues are due to the intra-cellular remodelling and cell intercalation. We here present a computational approach that can handle the two types of deformations, and also take into account the active cell response. The model resorts to cell-centred techniques, where particles represent cell nuclei, and to vertex models, where the vertices represent cell boundaries. This hybrid approach allows to consider separately intra-cellular and inter-cellular forces, and at the same time impose cell incompressibility.*

*In the proposed model, the cell boundaries (defined by vertices) and cell nuclei (or cell-centres) networks are coupled through an interpolation scheme, which is eventually relaxed in order to smooth the cell boundaries. We show that this coupling between the two networks modifies the equilibrium equations and stabilises the vertex network. Incompressibility is implemented through a penalty method. The resulting model can be implemented in two- and three-dimensions, and is complemented with active rheological models.*

*We apply the model to simulate the stretching and relaxation of cell monolayers, and to simulate wound healing process in the wing disc of *Drosophila* fly embryo. We show that the numerical results agree with the experimental measurements.*

## 1 INTRODUCTION

The development of computational models for studying the behaviour of biological tissue at cellular scale has progressively become a promising trend in modern biology. Due to the complexity of phenomena at cellular level, novel mechanical modelling is required to handle the observed tissue behaviour as well as being predictive to similar phenomena.

Due to the discrete nature of the tissue, and the relevance of the adhesive forces at the cell-cell junctions [2, 10] we resort to a cell-based approach which couples cell-centred [9] and vertex models [4, 8]. The two sets of points form two networks that we couple by using an appropriate interpolation. The combination of the two networks allows us modelling cellular rheology and adhesive forces in a joint manner, and inherit the advantages of cell-centres models (easy remodelling) and vertex models (explicit representation of boundary forces and area/volume preservation).

The developed model is employed to simulate embryogenesis of *Drosophila* wing disc [5] and a wound healing, which are experimentally analysed at the MRC-Laboratory for Molecular Cell Biology, at University College London. In this process, it is observed that the mechanical signalling and the activity of the stress fibres plays a predominant role, which is as determinant as the genetic and biochemical signalling.

We first describe the kinematic description of the network and the coupling between them. Two approaches for describing the cell boundaries are described: Voronoi and barycentric tessellation. We resort to the latter approach and justify our approach in Section 2. In Section 3 we deduce the mechanical equilibrium equations for arbitrary cell rheology. The latter is defined in Section 4, where we describe a specific viscoelastic model based on an evolution equation of the resting length. Some illustrative results are presented in Section 5, where we compare the experimental and computational deformations of the embryonic tissue.

## 2 CELL NETWORK DEFINITION

### 2.1 General approach

We concentrate our attention on flat monolayers where the cell deformations along the thickness direction is assumed constant, and thus our description is restricted to the two-dimensional case. Further extensions of the model to curved monolayers may be found in [6].

The cell-cell connectivity of the tissue is defined by a set of  $N$  nodes  $\mathbf{X} = \{\mathbf{x}_1 \dots \mathbf{x}_N\}$  that represent the cell nuclei (cell-centres) and a set of  $N_e$  bar elements connecting them and defined by a connectivity matrix  $\mathbf{C} = \{\mathbf{c}_1 \dots \mathbf{c}_{N_e}\}$ , with  $\mathbf{c}_e = \{i \ j\}^T$  and  $i$  and  $j$  the nodes the element  $e$  connects. We will resort here to a Delaunay triangulation [3, 1] in order to define the cell-cell connectivity. Since Delaunay triangulations form convex hulls of the set of nodes, we filter those triangles with very high or low aspect ratio. More precisely, we remove those triangles whose inradius  $r$  and circumradius  $R$  satisfy

$$\frac{r}{R} < \text{tol}_R$$

where  $\text{tol}_R$  is a tolerance here set to  $\text{tol}_R = 0.2$ .

Based on Delaunay triangulation, we use a tessellation defined by a set of  $N_v$  connected vertices  $\mathbf{V} = \{\mathbf{v}_1 \dots \mathbf{v}_{N_v}\}$ , which represent the cell-cell boundaries. We resort to two types of tessellations:

**Voronoi tessellation:** vertices form the Voronoi diagram of the Delaunay triangulation [1]. Unbounded Voronoi areas located at the boundary of the tissue are removed.

**Barycentric tessellation:** vertices are formed by the barycentres of the triangles. Each cell boundary is formed by joining the triangles that surround it, and external nodes do not form a cell.

Figure 1a-b shows the Delaunay triangulation and two tessellations described above. The vertices  $v_I$  of the two tessellations can be computed by using standard Finite Element interpolations  $N_i(\boldsymbol{\xi})$  of linear triangle elements as

$$\mathbf{v}_I = N_i(\boldsymbol{\xi}_I) \mathbf{x}_i \quad (1)$$

where summation is understood on the three nodes that form triangle  $I$  (see Figure 2). The interpolation parameter  $\boldsymbol{\xi}_I$  takes different values depending on the choice of the tessellation, and corresponds to the coordinate of vertex  $v_I$  in the reference element. In Voronoi tessellations,  $\boldsymbol{\xi}_I$  for each triangle can be computed from the actual position of  $v_I$  in the Voronoi diagram by solving a system of linear equations. In barycentric tessellations instead we have that  $\boldsymbol{\xi}_I = \{1/3, 1/3\}$  for all vertices.

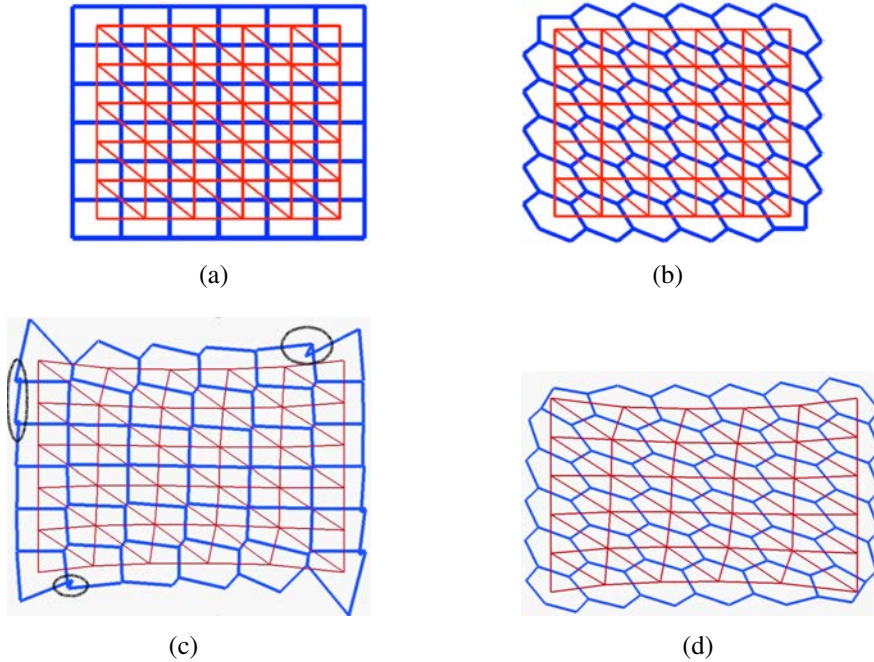


Figure 1: Triangulation and tessellation of a Cartesian  $5 \times 5$  mesh of nodes. (a) Delaunay triangulation and Voronoi tessellation. (b) Delaunay triangulation and barycentric tessellation. (c) Same triangulation and tessellation as in (b), but with an applied displacement on the nodes. Crossovers of original rectangular areas are indicated with brushed ellipses. (d) Same triangulation and tessellation as in (c), but with an applied displacement on the nodes.

We note that in Delaunay triangulations, Voronoi tessellations guarantee that the cells are convex, but we do not necessarily have that

$$\mathbf{v}_I \in T(\mathbf{x}_1, \mathbf{x}_2, \mathbf{x}_3), \quad (2)$$

with  $T(\mathbf{x}_1, \mathbf{x}_2, \mathbf{x}_3)$  the triangle formed by nodes  $\mathbf{x}_1$ ,  $\mathbf{x}_2$  and  $\mathbf{x}_3$ . Instead, vertices in barycentric tessellations satisfy the property in (2), although for very distorted meshes, cell centres may lay outside the cell boundary. More importantly though, if the value  $\boldsymbol{\xi}_I$  is kept constant, while the nodal positions  $\mathbf{x}_i$  are displaced, the Voronoi areas may easily yield non-convex polytopes or

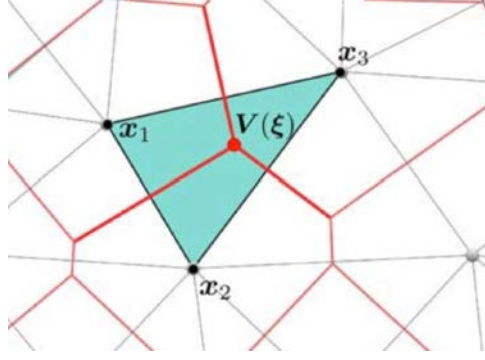


Figure 2: Schematic of the interpolation of the vertices on the Delaunay network.

with crossovers, giving rise to not valid tessellations, as Figure 2c shows. The displacement of the nodes with a constant interpolation parameter is considered in the next section. For this reason, only barycentric tessellations will be considered henceforth.

### 3 EQUILIBRIUM EQUATIONS

#### 3.1 Elastic potentials

Mechanical equilibrium is here considered by assuming an elastic potential for each bar of the Delaunay triangulation and also for each segment of the tessellation. More specifically, and for simplicity, the following quadratic elastic potentials for the Delaunay (D) and vertices in the tessellation (V) are considered:

$$\begin{aligned}\Psi_D(\mathbf{x}) &= \frac{1}{2}k_D \sum_e \varepsilon_e^2, \\ \Psi_V(\mathbf{x}, \boldsymbol{\xi}) &= \frac{1}{2}k_V \sum_E \varepsilon_E^2,\end{aligned}\tag{3}$$

where  $k_D > 0$  and  $k_V > 0$  are the material stiffness constants. The elastic strains  $\varepsilon_e$  and  $\varepsilon_E$  are defined by

$$\begin{aligned}\varepsilon_e &= \frac{l^{ij} - L^{ij}}{L^{ij}}, \\ \varepsilon_E &= \frac{l^{IJ} - L^{IJ}}{L^{IJ}}.\end{aligned}\tag{4}$$

where bar  $e$  joints nodes  $i$  and  $j$ , and segment  $E$  joints vertices  $I$  and  $J$ . The lengths  $l^{ij}$  and  $l^{IJ}$  are the current (deformed) lengths, while  $L^{ij}$  and  $L^{IJ}$  are the resting or reference lengths, that will be further explained in Section 4. The current lengths are defined by

$$\begin{aligned}l^{ij} &= \|\mathbf{x}^i - \mathbf{x}^j\|, \\ l_E^{IJ} &= \|\mathbf{v}^I - \mathbf{v}^J\|.\end{aligned}$$

We note that although  $l^{IJ}$  depends on the positions  $\mathbf{v}_I$ , due to interpolation (1), the elastic potential  $\Psi_V$  depends on the nodal positions  $\mathbf{x}_i$  and the parametric coordinates  $\boldsymbol{\xi} = \{\boldsymbol{\xi}_1, \dots, \boldsymbol{\xi}_{N_v}\}$ , as indicated in (3). Also, due to the non-linear dependence of the lengths on nodal and vertex coordinates, the elastic potentials are non-linear, even if the reference length  $L$  is constant.

### 3.2 Area preservation

In order to impose that the areas of the tessellation are preserved, the following penalty term is considered:

$$\Psi_A(\mathbf{x}, \boldsymbol{\xi}) = \frac{1}{2}k_A \sum_i (A_i - A_i^0)^2 \quad (5)$$

where  $k_A > 0$  is a penalty factor, and  $A_i$  and  $A_i^0$  are the current and initial areas, associated to each node  $i$  not located at the boundary. The areas  $A_i$  are in our case computed resorting to the divergence theorem and from the vertices positions surrounding each node  $i$ .

### 3.3 $\boldsymbol{\xi}$ -relaxation

In some occasions it becomes beneficial to relax the condition  $\boldsymbol{\xi}_I = \text{constant}$ . Indeed, as it will be shown in the next subsection, the interpolation in (1) implicitly prescribes the vertices' positions. This may have undesirable effects on the boundaries, and for this reason, the parametric coordinates of the vertices  $\boldsymbol{\xi}_I$  are allowed to vary. This is numerically achieved by adding at each time-step  $t_{n+1}$  a penalty term with the form

$$\Psi_\xi^{n+1}(\boldsymbol{\xi}) = \frac{1}{2}k_\xi \sum_I \|\boldsymbol{\xi}_I^{n+1} - \boldsymbol{\xi}_I^n\|^2. \quad (6)$$

with  $k_\xi > 0$  a penalty parameter, and the superscript  $n$  indicating quantities at time  $t_n$ . We note that after assigning the value  $k_\xi = \frac{\hat{k}_{x_i}}{\Delta t}$ , this penalty term is equivalent to adding a viscous term in the motion of the vertices with respect to the nodal positions  $\mathbf{x}_i$ .

### 3.4 Solution of equations

The equations of motion are solved at each time  $t_{n+1}$  by minimising the total potential

$$\Psi^{n+1}(\mathbf{x}, \boldsymbol{\xi}) = \Psi_D^{n+1}(\mathbf{x}) + \Psi_V^{n+1}(\mathbf{x}, \boldsymbol{\xi}) + \Psi_A^{n+1}(\mathbf{x}, \boldsymbol{\xi}) + \Psi_\xi^{n+1}(\boldsymbol{\xi}) \quad (7)$$

with respect to the nodal positions  $\mathbf{x}_i$  and parametric coordinates  $\boldsymbol{\xi}_I$ . This is equivalent to solving the following system of equations:

$$\begin{Bmatrix} \mathbf{g}_x \\ \mathbf{g}_\xi \end{Bmatrix} := \begin{Bmatrix} \nabla_x \Psi^{n+1} \\ \nabla_\xi \Psi^{n+1} \end{Bmatrix} = \mathbf{0} \quad (8)$$

We note that in the particular case that  $k_D > 0$  and  $k_V = k_A = k_\xi = 0$ , the previous set of equations is equivalent to solving the nodal equilibrium equations:

$$\frac{\partial \Psi_D(\mathbf{x})}{\partial \mathbf{x}_i} = \mathbf{0} \Rightarrow \sum_{e \in i} \mathbf{t}_{ei} = \mathbf{0}, \quad i = 1, \dots, N \quad (9)$$

with summation on all elements  $e$  connected to node  $i$ , and

$$\mathbf{t}_{ei} := k_D \varepsilon_e \frac{\partial \varepsilon_e}{\partial \mathbf{x}^i} \quad (10)$$

the traction force at node  $\mathbf{x}^i$  along the bar element  $\mathbf{c}^e = \{i j\}$ . Other expressions of  $\mathbf{t}_{ei}$  may be derived using more sophisticated elastic potentials  $\Psi_V(\boldsymbol{\xi})$  in (3). In the work presented here, the

non-linear rheology will be introduced in the next section by using a variable resting length  $L^{ij}$ . In the case  $k_V > 0$ , and using the interpolation in (1), we have the following non-zero term,

$$\nabla_x \Psi_V = \frac{\partial \Psi_V}{\partial \mathbf{v}_I} \frac{\partial \mathbf{v}_I}{\partial \mathbf{x}_i} = \frac{\partial \Psi_V}{\partial \mathbf{v}_I} \mathbf{P}_{Ii} \quad (11)$$

with

$$\mathbf{P}_{Ii} := \frac{\partial \mathbf{v}_I}{\partial \mathbf{x}_i} = N_i(\boldsymbol{\xi}_I) \mathbf{I}$$

When  $\boldsymbol{\xi}_I = \text{constant}$ , only the first block of equations in (8) needs to be solved. In this case, the system of equations in (9) turns into

$$\sum_{e \in i} \mathbf{t}_{ei} + \sum_{I \in i} \mathbf{P}_{Ii}^T \mathbf{t}_I = \mathbf{0}, \quad i = 1, \dots, N \quad (12)$$

with,

$$\mathbf{t}_I = \frac{\partial \Psi_V}{\partial \mathbf{v}_I} = k_V \varepsilon_e \frac{\partial \varepsilon_e}{\partial \mathbf{v}_I} \quad (13)$$

the traction at vertex  $I$  and with the second summation in (12) on all the vertices surrounding node  $i$ . The equation above reveals two consequences of the coupling: the nodal equilibrium equations have contribution from the vertices, and the interpolation in (1) modifies the tractions at the vertices  $\mathbf{t}_I$  through matrices  $\mathbf{P}_{Ii}$ . As a consequence, equilibrium at vertices is not fully preserved, even if  $k_D = 0$ . This fact has motivated the potential considered in the  $\boldsymbol{\xi}$ -relaxation.

When  $\boldsymbol{\xi}_I$  is allowed to vary, the second block of equations in (8) reads,

$$\left( \frac{\partial \Psi_V}{\partial \mathbf{v}_J} + \frac{\partial \Psi_A}{\partial \mathbf{v}_J} \right) \mathbf{Q}_{JI} + k_\xi (\boldsymbol{\xi}_I^{n+1} - \boldsymbol{\xi}_I^n) = \mathbf{0}, \quad I = 1, \dots, N_v$$

with

$$\mathbf{Q}_{JI} := \frac{\partial \mathbf{v}_J}{\partial \boldsymbol{\xi}_I} = \mathbf{x}_i \otimes \nabla N_i(\boldsymbol{\xi}_J) \delta_{IJ}$$

The non-linear equations are solved resorting to a Newton-Raphson scheme, which requires the computation of the Jacobian, which has the following general structure:

$$\mathbf{K} = \begin{bmatrix} \mathbf{K}_{xx} & \mathbf{K}_{x\xi} \\ \mathbf{K}_{\xi x} & \mathbf{K}_{\xi\xi} \end{bmatrix}$$

#### 4 CELL RHEOLOGY AND CONTRACTILITY

So far, only elastic forces are considered, and the sole time-dependent term is the  $\boldsymbol{\xi}$ -relaxation term, which is equivalent to a viscous force acting on the relative motion of vertices with respect to the nodes. We introduce here an additional viscous-like rheology by using the following evolution of the resting law:

$$\frac{\dot{L}}{L} = \gamma \varepsilon_e \quad (14)$$

where  $\gamma$  is the *remodelling rate*, and represents the ability of the tissue to adapt to the elastic strain. As shown in [7], this evolution law of the resting length induces a similar response to the Standard Maxwell model. Furthermore, it also allows simulating cell contractility by using a modified version of the law in (14) as

$$\frac{\dot{L}}{L} = \gamma(\varepsilon_e - \varepsilon_c) \quad (15)$$

where  $\varepsilon_c$  represents a contractile strain that the cell asymptotically aims to achieve. This law can be either applied to the bars at the Delaunay network and at the segments of the cell boundaries. This is implemented by, according to the strain definitions in (4), using the following expression in (10) and (13),

$$\begin{aligned} \frac{\varepsilon_e}{\mathbf{x}_i} &= \left( \frac{1}{L} - \frac{l^2}{L} \frac{\partial L}{\partial l} \right) \frac{\partial l}{\partial \xi_i} \\ \frac{\varepsilon_e}{\mathbf{x}_i} &= \mathbf{P}_{Ii}^T \left( \frac{1}{L} - \frac{l^2}{L} \frac{\partial L}{\partial l} \right) \frac{\partial l}{\partial \mathbf{v}_I} \end{aligned}$$

with

$$\begin{aligned} \frac{\partial l}{\partial \xi_i} &= \frac{1}{l}(\xi_i - \xi_j) \\ \frac{\partial l}{\partial \mathbf{v}_I} &= \frac{1}{l}(\mathbf{v}_I - \mathbf{v}_J) \end{aligned}$$

and computing  $\frac{\partial L}{\partial l}$  from a time-discretisation of the differential equation in (15).

## 5 RESULTS

The MRC-Laboratory for Molecular Cell Biology at University College London is currently experimentally analysing the wound healing process of embryonic tissues of *Drosophila* fly. In this process, the mechanical signalling and the activity of the stress fibres play a predominant role that is as important as the genetic and biochemical signalling.

The locations of the cells have been obtained from the phase contrast images, and the ablation of the tissue has been simulated by setting  $k_D = 0$  on those bars connected to ablated cells, and  $k_V = 0$  on those segments located at boundaries between dead cells.

We have resorted to the hybrid model in order to simulate the healing process. The material properties  $k_D$  and  $k_V$  have been fitted in order to match the evolution of the rate of the wound closure and the expansion after ablation. No areas preservation has been included, since this has not been found to be necessary.

The equations using  $\xi$ -relaxation have become necessary in order to avoid a zig-zag effect on the wound edge. Figure 3 compares the different wound profiles obtained without and with variation on parameter  $\xi$ . As it can be observed, the interpolation constraint has detrimental effects on the profile of the wound, which is smoothed after incrementally relaxing the positions of the vertices.

The wound closure is simulated by imposing a linearly incremental contractility  $\varepsilon_c$  at the wound edge. The sequence of wounded areas experimentally measured are compared to the numerical simulations in Figure 4. While the evolution and expansion of the wound and the trend of the closure fit the microscopic images, the model needs to be extended with remodelling capabilities in order to better simulate the final stages of the repairing process.

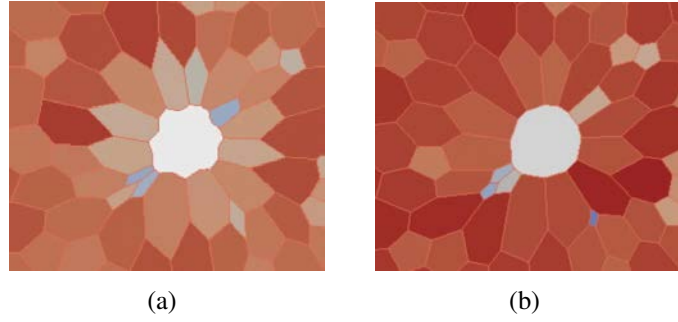


Figure 3: Effect of  $\xi$ -relaxation. (a) Wound edge without  $\xi$ -relaxation. (b) Wound edge applying  $\xi$ -relaxation.

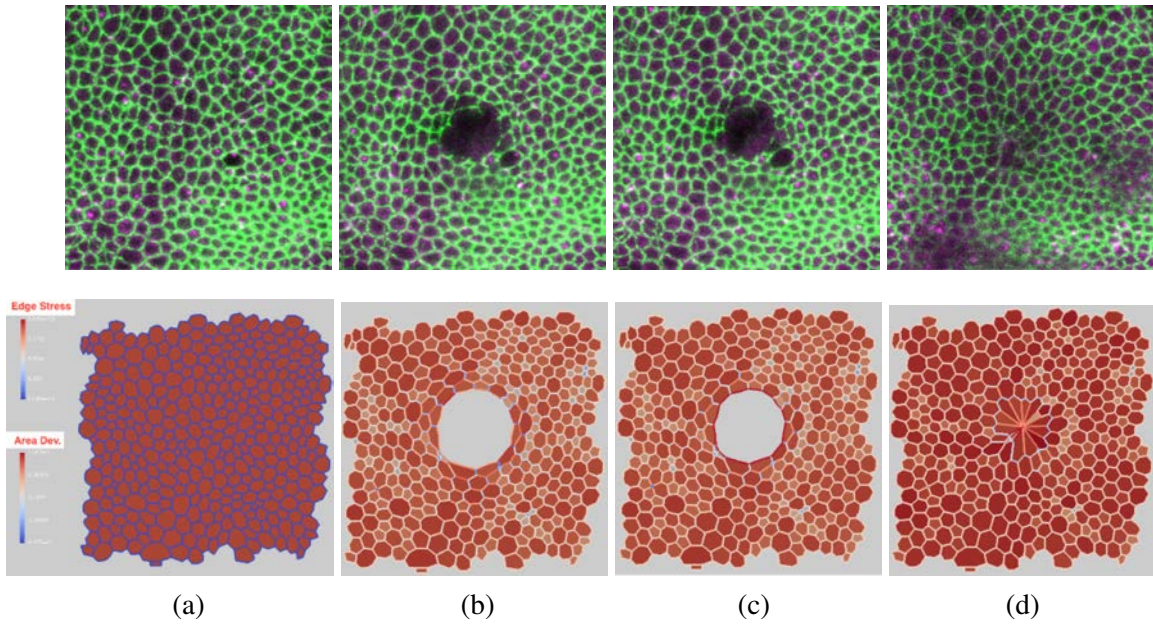


Figure 4: Response of tissue to applied damage by laser ablation of cells. Top: experimental images. Bottom: results of computational model. (a) Tissue before ablation, (b) Tissue recoil right after laser ablation applied. (c) Concentration of Myosin at the wound's edges causing wounds edge contractility. (d) Tissue after wound closure.

## 6 CONCLUSIONS

Wound closure of monolayers on elastic process has been well inspected [2]. However, the *in vivo* healing process is far more uncertain. The mechanical signalling and the tissue polarisation are currently solid hypotheses. These though have not been quantitatively measured or simulated.

By bridging the experimental measurements with rigorous mathematical and mechanical modelling we aim to couple the biochemical signalling and the forces exerted within the tissue. This understanding is necessary to predict tissue behaviour in other developmental processes and more generally in regenerative medicine.

The hybrid model and the numerical results presented here shows that the *in vivo* wound healing process can be successfully simulated. The model though requires to be complemented with remodelling capabilities. In order to inspect different mechanisms along the tissue thickness, it is also desirable to extend the model for the three-dimensional case. These features are currently investigated.

## REFERENCES

- [1] CB Barber, DP Dobkin, and H.T. HT Huhdanpaa. The Quickhull algorithm for convex hulls. *ACM Trans. Math.. Soft.*, 22(4):469–483, 1996. <http://www.qhull.org>.
- [2] A Brugués, E Anon, V Conte, JH Veldhuis, M Gupta, J Collombelli, J J Muñoz, GW Brodland, B Ladoux, and X Trepap. Forces driving epithelial wound healing. *Nature Phys.*, 10:683–690, 2014.
- [3] B. Delaunay. Sur la sphère vide. *Bull. Acad. Sc. URSS, cl. sc. math. nat.*, 6:793–800, 1934.
- [4] H. Honda, M. Tanemura, and T. Nagai. A three- dimensional vertex dynamics cell model of space-filling polyhedra simulating cell behavior in a cell aggregate. *J. Theor. Biol.*, 226:439–453, 2004.
- [5] Y. Mao, A.L. Tournier, A. Hoppe, L. Kester, B.J. Thompson, and N. Tapon. Differential proliferation rates generate patterns of mechanical tension that orient tissue growth. *EMBO J.*, 32(21):2790, 2803.
- [6] P. Mosaffa, N. Asadipour, D Millán, A. Rodríguez-Ferran, and J.J. Muñoz. Cell-centred model for the simulation of curved cellular monolayers . *Comp. Part. Mech.*, 2(4):359–370, 2015.
- [7] J.J. Muñoz and S. Albo. Physiology-based model of cell viscoelasticity. *Phys. Rev. E*, 88(1):012708, 2013.
- [8] S Okuda, Y Inoue, M Eiraku, Y Sasai, and T Adachi. Modeling cell proliferation for simulating three-dimensional tissue morphogenesis based on a reversible network reconnection framework. *Biomech. Model. Mechanobiol.*, 12:987–996, 2013.
- [9] P Pathmanathan, J Cooper, A Fletcher, G Mirams, P Murray, J Osborne, J Pitt-Francis, A Walter, and S J Chapman. A computational study of discrete mechanical tissue models. *Phys. Biol.*, 6:036001, 2009.
- [10] M Rauzi, P F Lenne, and T Lecuit. Planar polarized actomyosin contractile flows control epithelial junction remodelling. *Nature*, 468:1110–1114, 2010.